






Visualization of $4d$ orbital electrons in a pyrochlore-type oxide

Shunsuke Kitou ^{1,*} Yoshio Kaneko ¹ Yuiga Nakamura,² Kunihisa Sugimoto ³ Yusuke Nomura ⁴
Ryotaro Arita ^{1,5} Yoshinori Tokura,^{1,6,7} Hiroshi Sawa,⁸ and Taka-hisa Arima^{1,9}

¹*RIKEN Center for Emergent Matter Science, Wako 351-0198, Japan*

²*Japan Synchrotron Radiation Research Institute (JASRI), SPring-8, Hyogo 679-5198, Japan*

³*Department of Chemistry, Kindai University, Osaka 577-8502, Japan*

⁴*Department of Applied Physics and Physico-Informatics, Keio University, Yokohama 223-8522, Japan*

⁵*Research Center for Advanced Science and Technology, The University of Tokyo, Tokyo 153-8904, Japan*

⁶*Department of Applied Physics, The University of Tokyo, Tokyo 113-8656, Japan*

⁷*Tokyo College, The University of Tokyo, Tokyo 113-8656, Japan*

⁸*Department of Applied Physics, Nagoya University, Nagoya 464-8603, Japan*

⁹*Department of Advanced Materials Science, The University of Tokyo, Kashiwa 277-8561, Japan*



(Received 27 January 2023; revised 6 May 2023; accepted 6 July 2023; published 21 July 2023)

A real-space observation of the distribution state of valence electrons, which is responsible for physical properties, is a key methodology to understand the relation between the structure and functions of matter. Here, we observe Mo $4d$ orbital electrons at subangstrom resolution in a pyrochlore-type oxide $\text{Nd}_2\text{Mo}_2\text{O}_7$ based on the core differential Fourier synthesis (CDFS) analysis of high-energy x-ray diffraction data. The Mo^{4+} $4d^2$ orbital state is directly determined from the obtained valence electron density (VED) distribution. We also find a dip in the radial profile corresponding to a node of the $4d$ wave function. The VED distribution around the Nd site might be ascribed to the hybridization of neighboring O $2p$ with Nd $6s/6p/5d$ orbitals as well as the anisotropic Nd^{3+} $4f^3$ electrons, which cannot be reproduced by the simple $j-j$ or LS coupling pictures. In this paper, we demonstrate the usefulness of the CDFS analysis to investigate the orbital states in crystalline materials.

DOI: [10.1103/PhysRevB.108.024103](https://doi.org/10.1103/PhysRevB.108.024103)

I. INTRODUCTION

All physical properties are closely related to the orbital and spin states of valence electrons [1]. This concept is a starting point of condensed matter physics based on quantum mechanics. In magnetic transition-metal (rare-earth) compounds, the d (f) orbitals are partially occupied. The observation of the resultant anisotropic electron density (ED) distribution around the transition-metal (rare-earth) sites has been attracting attention. Several experimental methods have been proposed so far, such as polarized neutron diffraction [2], resonant x-ray scattering [3], multipole ED analysis [4] using x-ray diffraction (XRD), nonresonant inelastic x-ray scattering [5], higher-order harmonic generation of femtosecond laser pulse [6], and ultraviolet angle-resolved photoemission spectroscopy [7]. However, these methods are essentially a sort of parameter optimization and/or only provide information based on some quantum mechanical models. Furthermore, most of the previous reports on atomic orbital observations focused on $3d$ transition-metal compounds, which has a relatively weak spin-orbit coupling (SOC), and the results were in good agreement with a nonrelativistic theoretical model [2,3,5,8]. In the $4d$, $5d$, and $4f$ electron systems, more quantitative electron orbital observation is required due to the competition between

electron correlations, crystal field, SOC, and orbital hybridization. For instance, since the $4d$ orbitals have a spherical node corresponding to the phase switching point of the radial wave function, a dip structure should appear in the radial distribution of ED [Fig. 1(b)] in contrast to the $3d$ orbitals [Fig. 1(a)]. The $4f$ [Fig. 1(c)] and $5d$ orbitals may have more complicated anisotropy than the $3d$ orbitals because of the stronger SOC and/or the higher azimuthal quantum number. While these orbitals often play an important role in topics of recent great interest such as topological semimetal [9], multipolar ordering [10], magnetic skyrmion [11], and Kitaev quantum spin liquid [12], the real-space ED distribution has rarely been reported so far [13,14].

X-ray elastic scattering is a powerful method for observing real-space distribution of ED. For instance, with the ED analysis using the maximum entropy method (MEM) [15,16], we have succeeded in observing bonding electrons spreading spatially between atoms. Nevertheless, MEM without high-frequency (Q) data may not be very useful for analyzing ED around atoms where the ED steeply changes with position since the information entropy becomes maximal with the position-independent ED. On the contrary, the multipole ED analysis [4] may be useful for observing atomic orbital electrons. This analysis method is, however, dependent on the adopted model. One may get trapped at some local minima as in general optimization methods.

It is impossible in principle to extract the completely accurate ED distribution from the XRD data due to the truncation effect of the Fourier transform. However, the core differential

*Present address: Department of Advanced Materials Science, The University of Tokyo, Kashiwa 277-8561, Japan; kitou@edu.k.u-tokyo.ac.jp

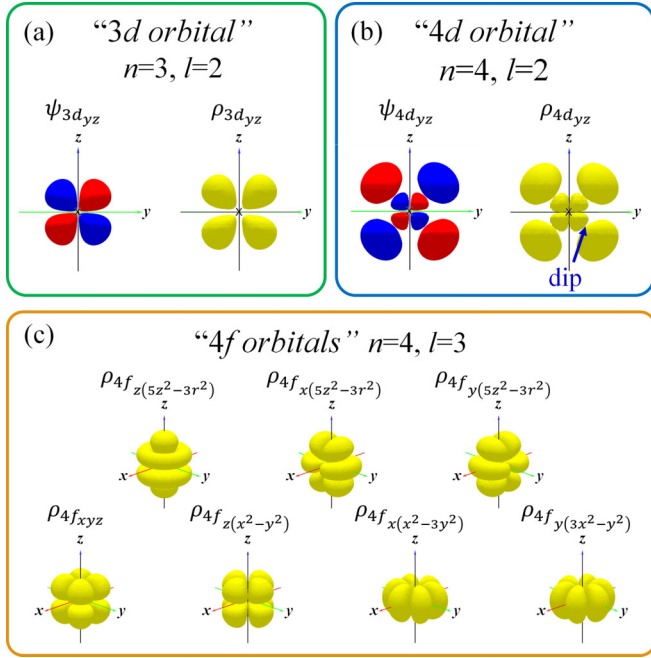


FIG. 1. Wave functions ψ (red and blue) and isodensity surfaces of electron density (ED) distribution $\rho (= |\psi|^2)$ (yellow) of (a) $3d_{yz}$ and (b) $4d_{yz}$ orbitals. Red and blue indicate positive and negative signs of the wave functions, respectively. (c) Isodensity surfaces of ED distribution for seven real $4f$ wave functions. n and l are the principal and azimuthal quantum numbers, respectively.

Fourier synthesis (CDFS) method [8] enables us to extract only valence electron contributions with a negligibly small truncation effect by subtracting the contribution of spherically symmetric core electrons from the total ED. The information required in advance is the radial distribution of the core ED around each constituent element. By combining high-photon-energy x rays obtained at a synchrotron radiation facility SPring-8 and the CDFS method, we succeeded in observing the bonding electrons in molecular solids [17–19] and the localized $3d$ electrons in transition-metal oxides [8,20]. High-photon-energy and high-intensity x rays allow us to perform XRD experiments on a small crystal of the order of tens of microns, reducing possible influences of absorption and dynamical diffraction.

We apply the CDFS method to pyrochlore-type $\text{Nd}_2\text{Mo}_2\text{O}_7$ [Fig. 2(a)] with the cubic space group $Fd\bar{3}m$ for studying the Nd $4f$ and Mo $4d$ orbitals. $\text{Nd}_2\text{Mo}_2\text{O}_7$ is a metallic compound and undergoes a ferromagnetic transition at ~ 90 K [21]. The formal valences of Nd and Mo are +3 and +4, resulting in the valence electron configurations of $4f^3$ and $4d^2$, respectively. The local symmetry at the Nd and Mo sites is $\bar{3}m$. Both Nd $4f^3$ and Mo $4d^2$ electrons are subject to electron-electron correlation, trigonal ligand field, and relativistic spin-orbit interaction. Each Mo atom is surrounded by six O(1) atoms to form a trigonally distorted octahedron [Fig. 2(b)], which are connected with each other by sharing a vertex to build a pyrochlore network of Mo atoms. Nd atoms form another pyrochlore network, while each of them is surrounded by eight O atoms [six O(1) and two O(2)] [Fig. 2(c)]. The MoO_6 octahedron shrinks along the trigonal axis, as reported

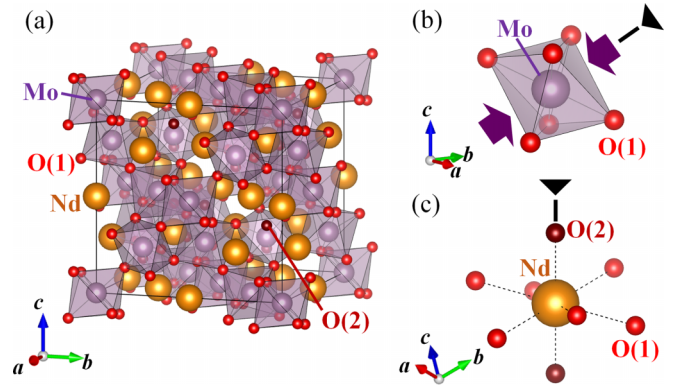


FIG. 2. (a) Crystal structure of $\text{Nd}_2\text{Mo}_2\text{O}_7$. (b) Compressive trigonal distortion of an MoO_6 octahedron. (c) Nd atom surrounded by eight O atoms [six O(1) and two O(2)]. Solid triangles in (b) and (c) indicate local threefold rotation axes.

previously [22]. The O(1)–Mo–O(1) angles are deviated by $6.96(4)^\circ$ from 90° (the structural parameters at 120 K are listed in Tables S1 and S2 in the Supplemental Material [23]). In the regular octahedral field, the $4d$ orbitals are split into the lower-lying triplet (t_{2g}) and the higher-lying doublet (e_g). The triplet is further split into a singlet (a_{1g}) and another doublet (e'_g) with the trigonal distortion of the octahedron. The ferromagnetic metal state is attributable to the double exchange interaction [26], if e'_g lies higher in energy than a_{1g} , where the Hund coupling works between the localized spin and conduction electron occupying the a_{1g} and e'_g orbitals, respectively.

$\text{Nd}_2\text{Mo}_2\text{O}_7$ exhibits an archetypal geometrical or topological Hall effect in the ferromagnetic phase, which is ascribed to the tiny noncoplanar canting of $4d$ moments [27–29]. Since the magnetic moment of Nd has a strong Ising anisotropy, the two-in/two-out type of magnetic order is realized on each regular tetrahedron formed by Nd atoms [30]. Then the Mo moments are also canted to host a scalar spin chirality because of the exchange interaction between Nd $4f$ and Mo $4d$ moments. The strong Ising anisotropy of the Nd moment is determined by the $J = \frac{9}{2}$ multiplet state of three $4f$ electrons in the trigonal crystal field. The pyrochlore molybdenite system undergoes a transition from a ferromagnetic metal to a spin-glass insulator by replacing Nd with rare-earth ions smaller than Gd [31]. It has been proposed that the spin-glass insulating state arises from the Mo orbital arrangement [32]. In short, the orbital states of Mo in the pyrochlore molybdenite play an essential role in the magnetic and transport properties. In this paper, we observed the spatial distribution of valence EDs (VEDs), which mainly occupy Nd $4f$, Mo $4d$, and O $2s/2p$ orbitals. It is noteworthy that some valence electrons may also occupy Nd empty $6s/6p/5d$ orbitals which are hybridized with O $2p$ orbitals.

II. METHODS

A. Synthesis

A single crystal of $\text{Nd}_2\text{Mo}_2\text{O}_7$ was synthesized by the following procedure. Nd_2O_3 powder was dried in air at 1000°C for 12 h. Nd_2O_3 and MoO_3 powders were mixed in the stoichiometric ratio. After grinding, the reaction product was pressed to form a rod and sintered in argon gas at 1400°C for

24 h. The rod was zone melted in a laser-floating zone furnace [33] in argon of 10 atm at 1700 °C. The molten zone was transferred at a speed of 10 mm/h to obtain a single-crystalline rod. Tiny crystals were obtained by crashing a part of the rod.

B. XRD experiments

The XRD experiments were performed on BL02B1 at a synchrotron facility SPring-8, Japan [34]. An N₂-gas-blowing device was employed to cool the crystal to 120 K in the paramagnetic phase. A two-dimensional detector CdTe PILATUS, which had a dynamic range of $\sim 10^7$, was used to record the diffraction pattern. The x-ray wavelength was $\lambda = 0.3100 \text{ \AA}$. The intensities of Bragg reflections of the interplane distance $d > 0.28 \text{ \AA}$ were collected by the CrysAlisPro program [35] using a fine slice method, in which the data were obtained by dividing the reciprocal lattice space region in increments of $\Delta\omega = 0.1^\circ$. Intensities of equivalent reflections were averaged, and the structural parameters were refined by using JANA2006 [36]. The structural refinement was performed using only the high-angle reflections, $\sin\theta/\lambda > 0.6 \text{ \AA}^{-1}$ (the so-called high-angle analysis). Since the contribution of spatially spread valence electrons is very small in the high-angle region (Fig. S8 in the Supplemental Material [23]), the structural parameters including the atomic displacement parameter (mainly due to the thermal vibration) are obtained with high accuracy.

C. Density functional theory calculation

To obtain the atomic scattering factors, we performed fully relativistic all-electron calculations based on density functional theory (DFT) for isolated Nd, Mo, and O atoms using QUANTUM ESPRESSO [37]. The Perdew-Burke-Ernzerhof functional [38] was employed to approximate the exchange-correlation functional. For Nd, we also performed the all-electron calculation for an isolated Nd³⁺ ion. We have summarized the comparison between our DFT calculations and available databases [39] in Supplemental Material Sec. 2 [23].

D. CDFS method

The CDFS method was used to extract the VED distribution around each atomic site [8]. [Xe]-, [Kr]-, and [He]-type electron configurations were regarded as core electrons for Nd, Mo, and O atoms, respectively. The contribution of the thermal vibration was subtracted from the VED using the atomic displacement parameters determined by the high-angle analysis [8]. The voxel size of the three-dimensional ED distribution is $\Delta V = 0.02 \text{ \AA}^3$. It should be noted that the absolute value of the obtained ED does not directly reproduce the number of valence electrons around the atoms, partly because the double scattering, absorption, extinction, and detector saturation [40] could not be completely excluded in the measurement of diffraction intensities. In addition, the analysis may suffer from the indefinite phase problem for weak reflections.

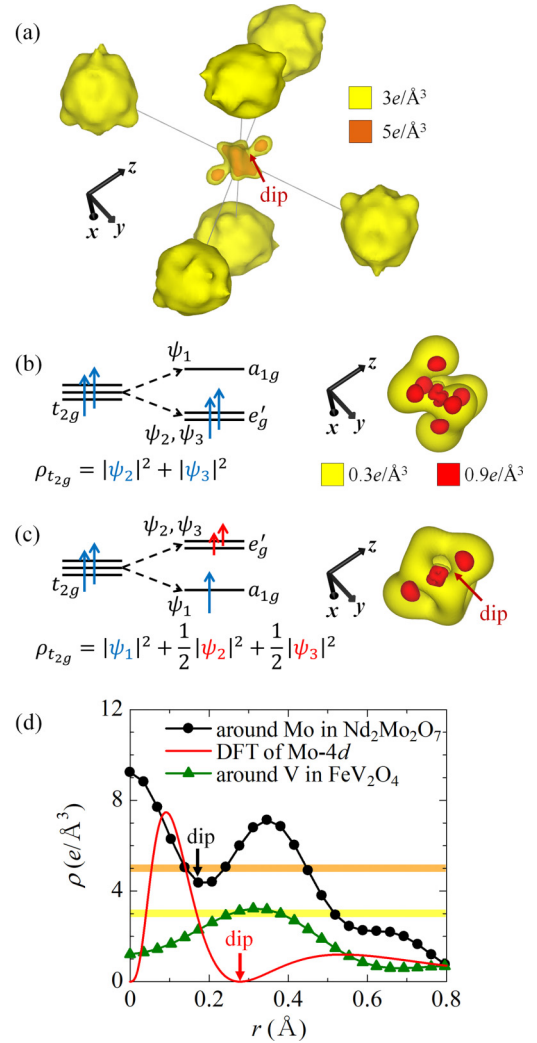


FIG. 3. (a) Valence electron density (VED) distribution around a MoO₆ octahedron obtained from the core differential Fourier synthesis (CDFS) analysis. (b) and (c) Two possible energy diagrams of the 4d *t*_{2g} orbital states and the simulated VED distributions. The *a*_{1g} singlet ψ_1 lies higher (lower) in energy than the *e*'_g doublet ψ_2 and ψ_3 in (b) [(c)]. Yellow, orange, and red surfaces show different electron density (ED) levels. (d) One-dimensional plots of the VEDs as functions of the distance *r* from the nucleus. Black dots show the 4d VED around the Mo site in the *z* direction obtained by the CDFS analysis. Horizontal yellow and orange lines indicate the ED levels corresponding to the surfaces shown by the same colors in (a). A red line shows the ED of a neutral Mo atom obtained by density functional theory (DFT) calculation, in which the ρ value is dependent on the direction and arbitrarily scaled here. Green triangles show the 3d VED around the V site in the direction of the local trigonal axis in spinel-type FeV₂O₄ with the cubic space group *Fd* $\bar{3}m$ (Ref. [20]).

III. RESULTS AND DISCUSSIONS

A. 4d² electrons around the Mo site

First, we focus on the Mo site. Figure 3(a) shows the spatial distribution of the VED around the MoO₆ octahedron obtained by the CDFS analysis. The local Cartesian coordinate system for the Mo site at (0, 0, 0) is defined as *x* $\parallel 2\mathbf{a} - \mathbf{b} - \mathbf{c}$, *y* $\parallel \mathbf{b} - \mathbf{c}$, and *z* $\parallel \mathbf{a} + \mathbf{b} + \mathbf{c}$. Here, the *z* axis corresponds

to the local threefold axis. The VED distributions around O(1) are roughly isotropic, which corresponds to the $2s^2 2p^6$ valence electrons. On the other hand, the VED distribution around Mo is observed to extend along the z axis. Two $4d$ electrons in an isolated trigonally distorted MoO_6 would be either of the $e_g'^2$ or $a_{1g}'e_g'^1$ state [Figs. 3(b) and 3(c)] if the SOC is neglected. The compressive distortion of the octahedron along the z axis [Fig. 2(b)] may prefer the latter state. Three basis functions of t_{2g} orbitals (see Fig. S12 in the Supplemental Material [23]) are described as

$$\psi_1 = \psi_{4d_{3z^2-r^2}}, \quad (1)$$

$$\psi_2 = \sqrt{\frac{2}{3}}\psi_{4d_{x^2-y^2}} + \sqrt{\frac{1}{3}}\psi_{4d_{zx}}, \quad (2)$$

$$\psi_3 = \sqrt{\frac{2}{3}}\psi_{4d_{xy}} - \sqrt{\frac{1}{3}}\psi_{4d_{yz}}. \quad (3)$$

Here, a_{1g} (e_g') corresponds to ψ_1 (ψ_2 and ψ_3). We here neglect the modulations in the coefficients $\sqrt{\frac{1}{3}}$ and $\sqrt{\frac{2}{3}}$ by the trigonal field. The VED of the $e_g'^2$ state, represented as $\rho_{t_{2g}} = |\psi_2|^2 + |\psi_3|^2$, does not extend along the z axis, as shown in Fig. 3(b). This anisotropy disagrees with the CDFS analysis of the experimental data. On the other hand, if one electron occupies a_{1g} and each orbital of ψ_2 and ψ_3 accommodates 0.5 electrons, the simulated VED distribution is expressed as $\rho_{t_{2g}} = |\psi_1|^2 + \frac{1}{2}|\psi_2|^2 + \frac{1}{2}|\psi_3|^2$. The VED extends along the z axis, as shown in Fig. 3(c), which is in good agreement with the CDFS result. The orbital state shown in Fig. 3(c) is also consistent with the double exchange scenario of the ferromagnetic metallic state [26].

Figure 3(d) shows a one-dimensional (1D) plot of the VED around the Mo site in the z direction (black dots) obtained by the CDFS analysis and the ED in the $4d$ orbital of an isolated neutral Mo atom (red line) calculated by DFT. In the experimental result, $\rho(r=0)$ is not zero, though the position at $r=0$ is a zero point of the $4d$ wave functions. The discrepancy may be ascribed to the insufficient spatial resolution of experimental data ($d_{\min} = 0.28 \text{ \AA}$) and the effect of the orbital hybridization with ligands [8]. As a reference for the $4d$ orbital, the 1D plot of the $3d$ VED around a V site along the threefold axis in spinel-type FeV_2O_4 at 160 K with the cubic space group $Fd\bar{3}m$ [20] obtained by the CDFS analysis is plotted by green triangles in Fig. 3(d). The V site has the same symmetry ($\bar{3}m$) and d -orbital configuration ($V^{3+} 3d^2: a_{1g}'e_g'^1$) as the Mo site in $\text{Nd}_2\text{Mo}_2\text{O}_7$. There is no dip in the VED around the V site, in contrast to the Mo site in $\text{Nd}_2\text{Mo}_2\text{O}_7$. The dip structure corresponding to the radial node of the $4d$ wave function is also confirmed in Figs. 3(a) and 3(c), where higher ED surfaces obtained by experiment (calculation) are shown by orange (red). By comparing the 1D plots between the CDFS analysis and the DFT calculation [Fig. 3(d)], we have found that the dip position of the experiment agrees with that of the DFT calculation within a difference of 0.1 \AA , suggesting a successful observation of the $4d$ orbital state including the node of the wave function. Another small dip structure can be found around $r = 0.5 \text{ \AA}$ (black dots), which does not exist in the DFT calculation. The deviation from the isolated atomic model may be related

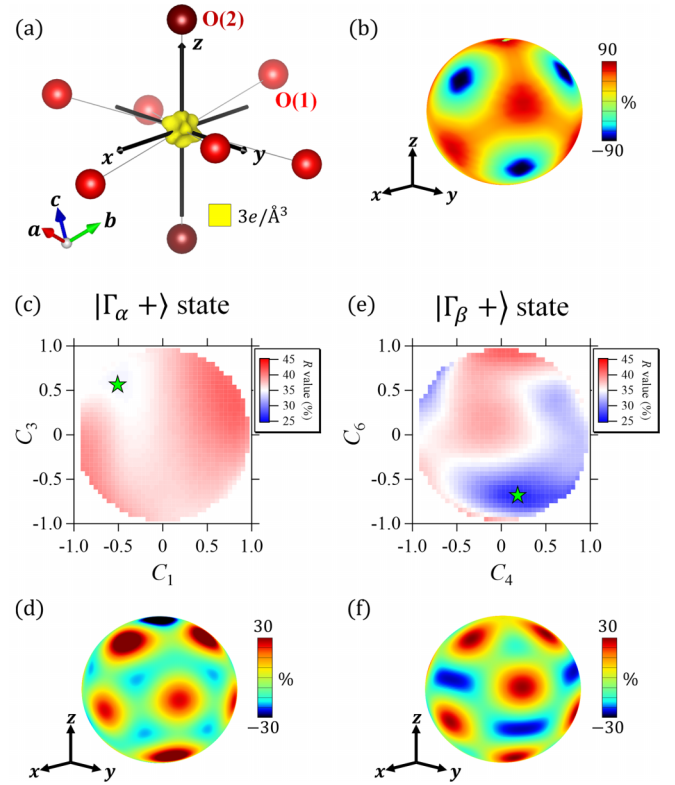


FIG. 4. (a) Valence electron density distribution around the Nd site obtained by the core differential Fourier synthesis (CDFS) analysis. (b) The electron density distribution $\rho(\theta, \phi)$ at a distance $r = 0.21 \text{ \AA}$ from the Nd site obtained by the CDFS analysis. Color maps of R values on two-dimensional (c) C_1 – C_3 ($C_2 \geq 0$) and (e) C_4 – C_6 ($C_5 \geq 0$) planes assuming $|\Gamma_\alpha^+\rangle$ and $|\Gamma_\beta^+\rangle$, respectively. Since the sign reversals of C_1 , C_2 , and C_3 (C_4 , C_5 , and C_6) do not change the wave function, we can select nonnegative C_2 (C_5) cases. Simulated surface color plots of $\rho_e(\theta, \phi)$ for (d) $|\Gamma_\alpha^+\rangle$ with $C_1 = -0.51$, $C_2 = 0.63$, and $C_3 = 0.59$, and (f) $|\Gamma_\beta^+\rangle$ with $C_4 = 0.15$, $C_5 = 0.70$, and $C_6 = -0.70$. These sets of wave function coefficients correspond to the positions of the green stars in (c) and (e), where R takes a local minimum of (d) 34.38% and (f) 26.15%, respectively. The color bar scale is plotted as $[\rho_e(\theta, \phi; \Gamma) - N_e]/N_e \times 100$. Here, $N_e = 3$, which is the number of $4f$ electrons.

to the intensity of $4d$ electrons, crystal electric field (CEF), and hybridization between neighboring atoms. This remains an open question.

B. VED around the Nd site

Next, we discuss the $4f^3$ VED distribution around the Nd site [Fig. 4(a)], in which a characteristic threefold anisotropy is observed. The distribution has higher ED in the directions of neighboring O atoms and at the nucleus position (Fig. S18 in the Supplemental Material [23]). There are two extreme schemes, i.e., j - j and LS coupling schemes, for considering the SOC in the $4f$ state (see Supplemental Material Sec. 4 [23]). In the j - j coupling scheme, the $4f^3$ ED is completely isotropic irrelevant to the CEF (Fig. S14 in the Supplemental Material [23]), which disagrees with the experimental result as shown in Fig. 4(a).

In the LS coupling scheme, since the total orbital and spin angular moments are $L = 6$ and $S = \frac{3}{2}$, respectively, the total angular momentum is $J = |L - S| = \frac{9}{2}$ for the $4f^3$ ground state. The isosurfaces of ED distributions $\rho_e(\mathbf{r}; J_z)$ and the square of the spherical harmonics terms $\rho_e(\theta, \phi; J_z)$ of each J_z state are shown in Figs. S15(a) and S15(b) in the Supplemental Material [23], which have clear anisotropy.

The $4f^3$ state in the trigonal field can be described as a linear combination of five Kramers doublets with different J_z states in the LS coupling scheme. The trigonal CEF \hat{H}_{CEF} can be expanded [41] as

$$\hat{H}_{\text{CEF}} = B_{20}\hat{O}_{20} + B_{40}\hat{O}_{40} + B_{43}\hat{O}_{43} + B_{60}\hat{O}_{60} + B_{63}\hat{O}_{63} + B_{66}\hat{O}_{66}. \quad (4)$$

Here, B_{lm} and \hat{O}_{lm} are the CEF parameters and the CEF operators, respectively. Then the $J = \frac{9}{2}$ multiplet should be split into five Kramers doublets. Each doublet can be represented as

$$|\Gamma_{\alpha\pm}\rangle = C_1 |J_z = \pm\frac{9}{2}\rangle + C_2 |J_z = \pm\frac{3}{2}\rangle + C_3 |J_z = \mp\frac{3}{2}\rangle, \quad (|C_1|^2 + |C_2|^2 + |C_3|^2 = 1), \quad (5)$$

or

$$|\Gamma_{\beta\pm}\rangle = C_4 |J_z = \pm\frac{7}{2}\rangle + C_5 |J_z = \pm\frac{1}{2}\rangle + C_6 |J_z = \mp\frac{5}{2}\rangle, \quad (|C_4|^2 + |C_5|^2 + |C_6|^2 = 1). \quad (6)$$

We optimize the coefficients C_i ($i = 1-6$) of the $|\Gamma_{\alpha+}\rangle$ or $|\Gamma_{\beta+}\rangle$ state to reproduce the anisotropy obtained by the CDFS analysis.

To extract the anisotropy in the calculated ED, the density at a distance $r = 0.21 \text{ \AA}$ from the Nd nucleus, which corresponds to the peak top of $\rho(r)$ obtained by the DFT calculation (Fig. S18(b) in the Supplemental Material [23]), is shown by a surface color plot on a sphere [Fig. 4(b)]. The color scale corresponds to the square of the spherical harmonics term $\rho(\theta, \phi)$ in the ED $\rho(\mathbf{r}) = \rho(r)\rho(\theta, \phi)$. We perform an optimization to determine the C_i coefficients in Eqs. (5) and (6). The R value for the fitting of $\rho(\theta, \phi)$ is defined as

$$R = \frac{\sum_{\theta, \phi} |\rho(\theta, \phi) - S\rho_e(\theta, \phi; \Gamma)|}{\sum_{\theta, \phi} |\rho(\theta, \phi)|}. \quad (7)$$

Here, $\rho_e(\theta, \phi; \Gamma)$ is the square of the spherical harmonics term in the Γ state calculated by Eq. (S1) in the Supplemental Material [23], and S is the scale factor.

The fitting results for each state are summarized in Figs. 4(c) and 4(e), respectively, and Table I. These states with the lowest R value (R_{min}) are shown as the surface color plots in Figs. 4(d) and 4(f), respectively. The $|\Gamma_{\beta+}\rangle$ state with a lower R value has an anisotropic $\rho_e(\theta, \phi)$, which is relatively like the experimental results [Fig. 4(b)]. However, $\rho_e(\theta, \phi)$ of the $|\Gamma_{\beta+}\rangle$ state cannot reproduce the upper and lower high densities observed in the experimental results. Also, the $|\Gamma_{\alpha+}\rangle$ state with a large $|J_z = \pm\frac{9}{2}\rangle$ component in-

TABLE I. Summary of fitting results of the VED around the Nd site.

| Model | C_1 or C_4 | C_2 or C_5 | C_3 or C_6 | R_{min} [%] |
|----------------------------|----------------|----------------|----------------|----------------------|
| $ \Gamma_{\alpha+}\rangle$ | -0.51 | 0.63 | 0.59 | 34.38 |
| $ \Gamma_{\beta+}\rangle$ | 0.15 | 0.70 | -0.70 | 26.15 |

stead of the $|\Gamma_{\beta+}\rangle$ state was obtained by inelastic neutron scattering experiments of $\text{Nd}_2\text{Zr}_2\text{O}_7$ [42], which has the same pyrochlore-type cubic ($F\bar{d}3m$) structure and in which Zr has no 4d electron. The incomplete simulation and the discrepancy between the Nd 4f states with different compounds suggest that the VED of Nd cannot be represented assuming a simple $4f^3$ state considering the SOC and the CEF. In fact, the ED extending along the z -axis direction may be due to electrons occupying the bonding orbitals formed by the hybridization between Nd $6s/6p/5d$ and O $2p$ orbitals because the Nd-O(2) bond [$2.2679(4) \text{ \AA}$] is shorter than the Nd-O(1) bond [$2.5632(9) \text{ \AA}$]. At present, there is no clear explanation for the discrepancy between the experimental results and the calculation in the LS coupling scheme. We are currently investigating the 4f VED distribution of other rare-earth pyrochlore compounds to address this issue from multiple perspectives. These results will be discussed in the near future.

IV. SUMMARY

The Mo 4d and Nd 4f orbital electrons in $\text{Nd}_2\text{Mo}_2\text{O}_7$ are successfully visualized by the CDFS analysis of the high-energy XRD data. The CDFS method only assumes core ED distribution when extracting the VED. The Mo 4d² ED distribution has a dip structure as predicted for the 4d orbitals with a radial node and corroborates with the $a_{1g}^1 e_g'^1$ configuration, which induces the double exchange interaction. The VED distribution around Nd has a complex anisotropy related to SOC, CEF, and orbital hybridization. This analysis method to observe the anisotropic VED with subangstrom resolution may pave the way to the detailed study of orbital physics.

ACKNOWLEDGMENTS

We thank T. Hara, Y. Hosogi, and T. Manjo for supporting synchrotron XRD experiments; K. Adachi, M. Hoshino, and D. Hashizume for in-house XRD characterization of crystal quality; and H. Kusunose, Y. Yamane, M. Hirschberger, and K. Kakurai for fruitful discussions. This paper was supported by a Grant-in-Aid for Scientific Research (Grants No. 19H05825, No. 22K14010, and No. 22H05145) from JSPS. The synchrotron radiation experiments were performed at SPring-8 with the approval of the Japan Synchrotron Radiation Research Institute (JASRI) (Proposals No. 2021A0070 and No. 2021B1261). Crystal structure and ED distribution were visualized by using VESTA [43].

[1] Y. Tokura and N. Nagaosa, Orbital physics in transition-metal oxides, *Science* **288**, 462 (2000).

[2] Y. Ito and J. Akimitsu, Observation of orbital ordering in K_2CuF_4 , *J. Phys. Soc. Jpn.* **40**, 1333 (1976).

- [3] Y. Murakami, J. P. Hill, D. Gibbs, M. Blume, I. Koyama, M. Tanaka, H. Kawata, T. Arima, Y. Tokura, K. Hirota *et al.*, Resonant X-Ray Scattering from Orbital Ordering in LaMnO_3 , *Phys. Rev. Lett.* **81**, 582 (1998).
- [4] N. K. Hansen and P. Coppens, Testing aspherical atom refinements on small-molecule data sets, *Acta Cryst.* **A34**, 909 (1978).
- [5] H. Yavaş, M. Sundermann, K. Chen, A. Amorese, A. Severing, H. Gretarsson, M. W. Haverkort, and L. H. Tjeng, Direct imaging of orbitals in quantum materials, *Nat. Phys.* **15**, 559 (2019).
- [6] J. Itatani, J. Levesque, D. Zeidler, H. Niikura, H. Pépin, J. C. Kieffer, P. B. Corkum, and D. M. Villeneuve, Tomographic imaging of molecular orbitals, *Nature (London)* **432**, 867 (2004).
- [7] P. Puschnig, S. Berkebile, A. J. Fleming, G. Koller, K. Emtsev, T. Seyller, J. D. Riley, C. Ambrosch-Draxl, F. P. Netzer, and M. G. Ramsey, Reconstruction of molecular orbital densities from photoemission data, *Science* **326**, 702 (2009).
- [8] S. Kitou, T. Manjo, N. Katayama, T. Shishidou, T. Arima, Y. Taguchi, Y. Tokura, T. Nakamura, T. Yokoyama, K. Sugimoto *et al.*, Collapse of the simple localized $3d^1$ orbital picture in Mott insulator, *Phys. Rev. Res.* **2**, 033503 (2020).
- [9] J. Hu, S. Y. Xu, N. Ni, and Z. Mao, Transport of topological semimetals, *Annu. Rev. Mater. Res.* **49**, 207 (2019).
- [10] P. Santini, S. Carretta, G. Amoretti, R. Caciuffo, N. Magnani, and G. H. Lander, Multipolar interactions in f -electron systems: The paradigm of actinide dioxides, *Rev. Mod. Phys.* **81**, 807 (2009).
- [11] Y. Tokura and N. Kanazawa, Magnetic skyrmion materials, *Chem. Rev.* **121**, 2857 (2021).
- [12] H. Takagi, T. Takayama, G. Jackeli, G. Khaliullin, and S. E. Nagler, Concept and realization of Kitaev quantum spin liquids, *Nat. Rev. Phys.* **1**, 264 (2019).
- [13] S. Pillet, G. Wu, V. Kulsomphob, B. G. Harvey, R. D. Ernst, and P. Coppens, Investigation of Zr–C, Zr–N, and potential agostic interactions in an organozirconium complex by experimental electron density analysis, *J. Am. Chem. Soc.* **125**, 1937 (2003).
- [14] C. Gao, A. Genoni, S. Gao, S. Jiang, A. Soncini, and J. Overgaard, Observation of the asphericity of $4f$ -electron density and its relation to the magnetic anisotropy axis in single-molecule magnets, *Nat. Chem.* **12**, 213 (2020).
- [15] M. Takata, B. Umeda, E. Nishibori, M. Sakata, Y. Saito, M. Ohno, and H. Shinohara, Confirmation by x-ray diffraction of the endohedral nature of the metallofullerene $\text{Y}@\text{C}_{82}$, *Nature (London)* **377**, 46 (1995).
- [16] E. Nishibori, E. Sunaoshi, A. Yoshida, S. Aoyagi, K. Kato, M. Takata, and M. Sakata, Accurate structure factors and experimental charge densities from synchrotron x-ray powder diffraction data at SPring-8, *Acta Cryst.* **A63**, 43 (2007).
- [17] S. Kitou, T. Fujii, T. Kawamoto, N. Katayama, S. Maki, E. Nishibori, K. Sugimoto, M. Takata, T. Nakamura, and H. Sawa, Successive Dimensional Transition in $(\text{TMTTF})_2\text{PF}_6$ Revealed by Synchrotron X-ray Diffraction, *Phys. Rev. Lett.* **119**, 065701 (2017).
- [18] S. Kitou, Y. Hosogi, R. Kitaura, T. Naito, T. Nakamura, and H. Sawa, Direct observation of molecular orbitals using synchrotron x-ray diffraction, *Crystals* **10**, 998 (2020).
- [19] S. Kitou, T. Tsumuraya, H. Sawahata, F. Ishii, K. Hiraki, T. Nakamura, N. Katayama, and H. Sawa, Ambient-pressure Dirac electron system in the quasi-two-dimensional molecular conductor α -(BETS) $_2\text{I}_3$, *Phys. Rev. B* **103**, 035135 (2021).
- [20] T. Manjo, S. Kitou, N. Katayama, S. Nakamura, T. Katsufuji, Y. Nii, T. Arima, J. Nasu, T. Hasegawa, K. Sugimoto *et al.*, Do electron distributions with orbital degree of freedom exhibit anisotropy? *Mater. Adv.* **3**, 3192 (2022).
- [21] N. Ali, M. P. Hill, S. Labroo, and J. E. Greedan, Magnetic and electrical properties of $\text{R}_2\text{Mo}_2\text{O}_7$ pyrochlore compounds, *J. Solid State Chem.* **83**, 178 (1989).
- [22] Y. Moritomo, S. Xu, A. Machida, T. Katsufuji, E. Nishibori, M. Takata, M. Sakata, and S-W. Cheong, Chemical pressure control of exchange interaction in Mo pyrochlore, *Phys. Rev. B* **63**, 144425 (2001).
- [23] See Supplemental Material at <http://link.aps.org/supplemental/10.1103/PhysRevB.108.024103> for the results of crystal structural analysis, atomic scattering factor calculated by DFT, definition of quantization axes, and VED of $\text{Nd}^{3+} 4f^3$, which includes Refs. [24,25].
- [24] H. Kusunose, Description of multipole in f -electron systems, *J. Phys. Soc. Jpn.* **77**, 064710 (2008).
- [25] T. Hotta and H. Harima, Effective crystalline electric field potential in a j - j coupling scheme, *J. Phys. Soc. Jpn.* **75**, 124711 (2006).
- [26] P. W. Anderson and H. Hasegawa, Considerations on double exchange, *Phys. Rev.* **100**, 675 (1955).
- [27] Y. Taguchi, Y. Oohara, H. Yoshizawa, N. Nagaosa, and Y. Tokura, Spin chirality, Berry phase, and anomalous Hall effect in a frustrated ferromagnet, *Science* **291**, 2573 (2001).
- [28] Y. Taguchi, T. Sasaki, S. Awaji, Y. Iwasa, T. Tayama, T. Sakakibara, S. Iguchi, T. Ito, and Y. Tokura, Magnetic Field Induced Sign Reversal of the Anomalous Hall Effect in a Pyrochlore Ferromagnet $\text{Nd}_2\text{Mo}_2\text{O}_7$: Evidence for a Spin Chirality Mechanism, *Phys. Rev. Lett.* **90**, 257202 (2003).
- [29] M. Hirschberger, Y. Nomura, H. Mitamura, A. Miyake, T. Koretsune, Y. Kaneko, L. Spitz, Y. Taguchi, A. Matsuo, K. Kindo *et al.*, Geometrical Hall effect and momentum-space Berry curvature from spin-reversed band pairs, *Phys. Rev. B* **103**, L041111 (2021).
- [30] Y. Yasui, Y. Kondo, M. Kanda, M. Ito, H. Harashina, M. Sata, and K. Kakurai, Magnetic structure of $\text{Nd}_2\text{Mo}_2\text{O}_7$, *J. Phys. Soc. Jpn.* **70**, 284 (2001).
- [31] N. Hanasaki, K. Watanabe, T. Ohtsuka, I. Kézsmárki, S. Iguchi, S. Miyasaka, and Y. Tokura, Nature of the Transition between a Ferromagnetic Metal and a Spin-Glass Insulator in Pyrochlore Molybdates, *Phys. Rev. Lett.* **99**, 086401 (2007).
- [32] K. Mitsumoto, C. Hotta, and H. Yoshino, Spin-Orbital Glass Transition in a Model of a Frustrated Pyrochlore Magnet without Quenched Disorder, *Phys. Rev. Lett.* **124**, 087201 (2020).
- [33] Y. Kaneko and Y. Tokura, Floating zone furnace equipped with a high power laser of 1kW composed of five smart beams, *J. Cryst. Growth* **533**, 125435 (2020).
- [34] K. Sugimoto, H. Ohsumi, S. Aoyagi, E. Nishibori, C. Moriyoishi, Y. Kuroiwa, H. Sawa, and M. Takata, Extremely high resolution single crystal diffractometry for orbital resolution using high energy synchrotron radiation at SPring-8, *AIP Conf. Proc.* **1234**, 887 (2010).
- [35] *CrysAlisPro* (Agilent Technologies Ltd, Yarnton, 2014).

- [36] V. Petříček, M. Dušek, and L. Palatinus, Crystallographic computing system JANA2006: General features, *Z. Kristallogr. Cryst. Mater.* **229**, 345 (2014).
- [37] P. Giannozzi, O. Andreussi, T. Brumme, O. Bunau, M. B. Nardelli, M. Calandra, R. Car, C. Cavazzoni, D. Ceresoli, M. Cococcioni *et al.*, Advanced capabilities for materials modeling with QUANTUM ESPRESSO, *J. Phys.: Condens. Matter* **29**, 465901 (2017).
- [38] J. P. Perdew, K. Burke, and M. Ernzerhof, Generalized Gradient Approximation Made Simple, *Phys. Rev. Lett.* **77**, 3865 (1996).
- [39] Z. Su and P. Coppens, Relativistic x-ray elastic scattering factors for neutral atoms $Z = 1-54$ from multiconfiguration Dirac-Fock wavefunctions in the $0-12 \text{ \AA}^{-1} \sin\theta/\lambda$ range, and six-Gaussian analytical expressions in the $0-6 \text{ \AA}^{-1}$ range, *Acta Cryst.* **A53**, 749 (1997); P. Macchi and P. Coppens, Relativistic analytical wave functions and scattering factors for neutral atoms beyond Kr and for all chemically important ions up to Γ^- , *ibid.* **A57**, 656 (2001).
- [40] L. Krause, K. Tolborg, T. B. E. Gronbech, K. Sugimoto, B. B. Iversen, and J. Overgaard, Accurate high-resolution single-crystal diffraction data from a Pilatus3 X CdTe detector, *J. Appl. Cryst.* **53**, 635 (2020).
- [41] M. T. Hutchings, Point-charge calculations of energy levels of magnetic ions in crystalline electric fields, *Solid State Phys.* **16**, 227 (1964).
- [42] J. Xu, V. K. Anand, A. K. Bera, M. Frontzek, D. L. Abernathy, N. Casati, K. Siemensmeyer, and B. Lake, Magnetic structure and crystal-field states of the pyrochlore antiferromagnet $\text{Nd}_2\text{Zr}_2\text{O}_7$, *Phys. Rev. B* **92**, 224430 (2015).
- [43] K. Momma and F. Izumi, VESTA 3 for three-dimensional visualization of crystal, volumetric and morphology data, *J. Appl. Crystallogr.* **44**, 1272 (2011).